Intermetallics 145 (2022) 107560

Contents lists available at ScienceDirect

Intermetallics

journal homepage: www.elsevier.com/locate/intermet

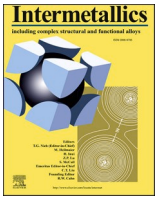

Using characteristic structural motifs in metallic liquids to predict glass forming ability

W. Porter Weeks [a,*], Katharine M. Flores [a,b]

[a] Institute of Materials Science and Engineering, Washington University in St. Louis, St. Louis, MO, 63130, USA
[b] Department of Mechanical Engineering and Materials Science, Washington University in St. Louis, St. Louis, MO, 63130, USA

ARTICLE INFO

Keywords:
Metallic glass
Molecular dynamics simulations
Amorphous materials
Glass forming ability

ABSTRACT

Despite intense interest in the discovery and design of metallic glasses, the efficient *a priori* identification of novel glass-formers without the need for time-consuming experimental characterization has remained an unattained goal. To address this, we use geometric alignment and density-based clustering algorithms to quantitatively describe the short-range atomic structure in the simulated liquid state for five known metallic glass-forming systems. We show that each liquid is comprised of a surprisingly small number of geometrically-similar atomic clusters (6–8 characteristic motifs in the systems studied) and that the variance of the population distribution of these clusters in the high temperature liquid is inversely correlated to the experimentally-observed glass-forming ability (GFA) as a function of composition within each system studied. These correlations are observed without consideration of temperature-dependent evolution or longer range atomic arrangements, which are much more time-consuming to evaluate. The relative simplicity and broad applicability of this technique to both good glass-forming systems (Cu–Zr, Ni–Nb, Al–Ni–Zr) and poor glass-forming systems (Al–Sm, Au–Si) suggests that the population of characteristic atomic clusters in the simulated liquid could be used as an efficient, high-throughput screening method for identification of potential glass-forming alloys.

1. Introduction

Metallic glasses, including "bulk" metallic glasses able to be cast with dimensions larger than 1 mm, have been the subject of intense study since their discovery [1–4] predominantly due to desirable mechanical properties such as high elastic strain limit, near-theoretical strengths, and thermoplastic formability [5,6]. A major focus of this research has been attempting to develop *a priori* predictors of glass-forming ability (GFA) in metallic alloys such that time-consuming experiments are not the limiting factor to the discovery of alloys amenable to glass formation. Parameters based on critical temperatures including the glass transition temperature (T_g), liquidus temperature (T_l), and crystallization temperature (T_x), such as the reduced glass transition temperature ($T_{rg} = T_g/T_l$) and degree of undercooling ($\Delta T_x = T_x - T_g$), have been proposed, although these parameters require prior knowledge of the glass transition temperature, and trends in T_{rg} and ΔT_x do not effectively scale with critical casting thickness across metallic systems [7–13]. The early research of Bernal [14,15] and Gaskell [16] led to structural approaches based on atomic identities or atomic radius ratios of components such as the efficient cluster packing (ECP) model [17–21]. While the ECP model has been of particular interest, it provides little explanation of why certain compositions *within* a given alloy system are better glass-formers than surrounding compositions and has limited ability to differentiate among systems that exhibit different GFA despite containing components of similar atomic radii (e.g. Ni-Zr and Cu–Zr) [20]. The deficiencies in the aforementioned approaches have led to a general lack of understanding about why certain metallic alloy compositions are better glass-formers than others.

More recently, Mauro et al. found that the kinetic fragility of the high-temperature liquid is strongly correlated to the ordering observed near T_g [22], leading to an increased interest in the characterization of metallic liquids, particularly their short-range and medium-range order (SRO/MRO). The SRO and MRO of metallic liquids [23–26] as well as the temperature-dependent evolution of these structures [27] have been investigated experimentally, although the inherent challenges associated with the experimental characterization of metallic liquids has led to a focus on the analysis of simulated materials. Structural analysis techniques such as Bond Orientation Order (BOO) [28–36], Honeycutt-Andersen's common neighbor analysis (CNA) [37–43], and Voronoi tessellation [21,44–47] have been applied to this problem. Voronoi

* Corresponding author.
E-mail address: weekswp@wustl.edu (W.P. Weeks).

https://doi.org/10.1016/j.intermet.2022.107560
Received 29 December 2021; Received in revised form 2 March 2022; Accepted 28 March 2022
Available online 5 April 2022

tessellation, in particular, allows for the direct comparison of local volumes in the simulation cell through Voronoi indices $< i_3,i_4,i_5,i_6 >$, corresponding to the number of faces with 3, 4, 5, or 6 vertices present on the polyhedron representative of a given local volume. Most notably, the presence of fully icosahedral $<0,0,12,0>$ Voronoi clusters has been shown to correlate with high GFA in Cu–Zr alloys [22,45,48,49].

While Voronoi tessellation, BOO, and CNA are in common usage, potential issues with these methods has led to the recent development of novel structural analysis tools such as that proposed by Fang et al. [50–52] and a geometry-based combination of Point-Pattern Matching [53] and a density-based machine learning clustering algorithm (HDBSCAN) [54]. All of these techniques have contributed to the growing knowledge surrounding the SRO/MRO present in simulated metallic liquids [26,51,55–61], the evolution of these structures with temperature [51,55,57,58,60,61], and crystal nucleation and growth [35,59,62,63]. While this previous research has led to improved understanding of the glass formation process, consideration of these factors requires extensive computation and does not lend itself to the high-throughput discovery of high-GFA alloys, which is the goal of this work.

Recently, Wang et al. showed that the variance of the population fraction of atomic clusters with different Voronoi indices in the simulated liquid is inversely correlated to GFA in a range of ternary metallic systems [47]. This suggests that alloys with poor GFA exhibit more order in the simulated liquid than high-GFA alloys [47], and that a simple, reliable descriptor of such order could be used for the discovery of new glass-forming systems, without the need for a time- and resource-consuming quench. However, recent papers [50,51,53,54,64–68] have raised questions about the ability of Voronoi tessellation to effectively describe the geometric configuration of atomic clusters, limiting its reliability as an indicator of GFA.

In this paper, we build on the work of Wang et al. to show that an alternative method for the characterization of the simulated liquid structure [53,54] identifies the best experimental glass-forming compositions in several metallic systems including Cu-Zr [69–75], Ni-Nb [76–79], Al-Sm [66,80–85], Au-Si [4,86], and Al–Ni–Zr [47,87], with Al–Sm and Au–Si being poor glass-forming systems relative to the other three. Moreover, we show that this alternative structural analysis is a more effective way to quantitatively describe the short-range geometric configurations of atomic clusters in the liquid than Voronoi tessellation. While factors such as MRO, temperature-dependent structural evolution, and the kinetics of crystal nucleation and growth also have significant effects on glass formation, this work suggests that SRO in the liquid state alone can be used as a coarse identifier of glass-forming regions in a wide variety of metallic systems. In combination with the relative ease of calculation, the seemingly broad applicability of this approach makes it a promising method for the high-throughput identification of novel glass-formers.

2. Methods

2.1. Molecular dynamics simulations of liquid structures

The analysis discussed in this paper arises from MD simulations of structures in each of the relevant alloy systems (Cu–Zr, Ni–Nb, Al–Sm, Au–Si, and Al–Ni–Zr) using the Large-scale Atomic/Molecular Massively Parallel Simulator (LAMMPS) [88]. First, valid interatomic potentials were identified for each of the alloy systems. Widely applicable Finnis-Sinclair (FS) interatomic potentials were identified for Cu-Zr [89], Ni-Nb [78], and Al–Ni–Zr [90] while more narrow potentials were identified for Al-Sm [91] and Au–Si [92] alloys, where the latter two have been proven accurate for Al-rich and Au-rich alloys, respectively. The lack of widely applicable potentials for Al–Sm and Au–Si limited the compositional range that could be investigated within these systems, but the valid composition range overlaps with known glass-formers, enabling comparison with experimental results.

Table 1
Starting structures used to construct MD simulation cells for the investigated systems.

Alloy System	Starting Structure	Space Group	Lattice Parameters (Angstroms)	Expanded Supercell Size (# of atoms)
Cu–Zr*	Cu_5Zr	216	a, b, c = 6.838	34,992
Ni–Nb	Ni_3Nb	225	a, b, c = 5.850	32,000
Al–Sm	AlSm	221	a, b, c = 3.677	31,250
Au–Si	Au_3Si	225	a, b, c = 6.571	35,152
Al–Ni–Zr*	Zr_5Ni_4Al	84	a,b = 7.205; c = 6.646	34,560
*Ni–Zr	Ni_5Zr	216	a,b,c = 4.773	32,400
*Pure Cu	FCC Cu	225	a, b, c = 3.621	32,000
*Pure Zr	FCC Zr	225	a, b, c = 4.536	32,768

*Different structures were used for pure Cu, pure Zr, and the Ni–Zr binary compositions of the Al–Ni–Zr system due to the instability observed when using the Cu_5Zr as the starting structure for these compositions.

Table 2
Equilibration temperatures (T_1 and T_2), cooling rates ($R_{1,2}$ and $R_{2,eval}$), temperature step during cooling (dT), and the temperature at which the liquid structure was evaluated (T_{eval}) for each system investigated.

System	T_1 (K)	$R_{1,2}$ (K/sec)	T_2 (K)	dT (K)	$R_{2,eval}$ (K/sec)	T_{eval} (K)
Cu–Zr	2700	3.33×10^{10}	2600	50	3.5×10^{11}	1450
Ni–Nb	3000	4.99×10^{10}	2850	50	3.5×10^{11}	2300
Al–Sm	2000	4.99×10^{10}	1850	25	1.75×10^{11}	1750/1000
Au–Si	2500	1.66×10^{11}	2000	30	2.09×10^{11}	1760
Al–Ni–Zr	2700	3.33×10^{10}	2600	50	3.5×10^{11}	1800

Structures were simulated in increments of 5 at. % or finer across the composition range of interest for binary systems and increments of 10 at % or finer for the Al–Ni–Zr system. For each composition, stable starting structures were identified and expanded to supercells larger than 30,000 atoms; the details of the starting structures are provided in Table 1. Atomic identities were then randomly assigned in the proper proportions for a given composition.

All simulations were performed in an NPT ensemble at a constant pressure of 1 bar, and the simulated cooling rates were justified by prior research on the simulation of metallic materials [93]. The simulation parameters for each system are specified in Table 2. The starting structures were rapidly heated to a system-specific temperature, T_1, far above the liquidus temperature, and allowed to equilibrate for 600 ps. They were then cooled to a system-specific lower temperature, T_2, at a constant rate ($R_{1,2}$) over 3000 ps. Finally, the structures were slowly cooled in a step-wise fashion (dT) at a system-specific rate ($R_{2,eval}$), equilibrating for 428 ps at each temperature, to the temperature of interest for the analysis, T_{eval}. T_{eval} was chosen to be 50–100° above the known liquidus temperature for most compositions of interest within the system and was held constant. For some compositions near high melting point end-members, the rapidly increasing liquidus meant that T_{eval} was lower than the known liquidus temperature (i.e. $Cu_{20}Zr_{80}$–Cu_0Zr_{100}, $Ni_{20}Nb_{80}$–Ni_0Nb_{100}). In these cases, it was confirmed that the simulated structure at T_{eval} had not undergone a discontinuity in the evolution of atomic density with cooling, indicative of crystallization. Note further that two evaluation temperatures were investigated for Al–Sm due to the rapidly changing liquidus temperature in this system; these results are compared below. The choice to hold T_{eval} constant throughout each analysis means that specific compositions were investigated at different temperature excursions relative to the local liquidus. This was done to ensure that all of the simulated structures within a given system were

prepared under consistent conditions, (i.e. same geometric starting structure, same number of timesteps, same cooling rates, etc.). Moreover, evaluating the structures at the same temperature ensures that the thermal energy and thus atomic mobility is approximately constant across all compositions. Finally, using a constant T_{eval} accelerates the analysis, in keeping with the high-throughput nature of the investigation.

2.2. Analysis of liquid structure

The structures of the simulated liquids were analyzed using two different methods. The first used the OVITO® visualization software [94] to determine the population of Voronoi clusters with unique indices. We then calculated the variance of this cluster population as described below, following the example of Wang et al. [47].

The second technique utilized a combination of Point-Pattern Matching (PPM) alignment [53] and Hierarchal Density-Based Spatial Clustering of Applications with Noise (HDBSCAN) [95], a machine learning-based clustering algorithm, to identify atomic-scale clusters with "similar" structures. While the procedure used for this technique is heavily based upon that of Maldonis et al. [54], whose codes are publicly available [96], slight alterations to the code and major alterations to the workflow were necessary for the purposes of the present work. These modified codes are publicly available in the form of a GitHub repository [97]. Each simulated liquid was split into C local atomic environments (clusters) each centered on an atom in the simulation cell and including the atoms within a radius equivalent to the position of the first minimum in the periodic distribution function calculated for the liquid. To determine how similar these clusters are to one another, we utilize PPM alignment [53]. From the atomic arrangements within any two clusters (A and B), we calculate the following values, which compare the local geometric arrangement of the atoms in the clusters [54]:

$$L^2 = \frac{1}{n}\sqrt{\sum_{i=0}^{n}(A_{ix}-B_{ix})^2+(A_{iy}-B_{iy})^2+(A_{iz}-B_{iz})^2} \quad (1)$$

$$L^1 = \frac{1}{n}\sum_{i=0}^{n}|A_{ix}-B_{ix}|+|A_{iy}-B_{iy}|+|A_{iz}-B_{iz}| \quad (2)$$

$$L^\infty = \max\left(|A_{ix}-B_{ix}|+|A_{iy}-B_{iy}|+|A_{iz}-B_{iz}|\right) \quad (3)$$

$$L^\measuredangle = \frac{1}{m}\sum_{i,j}|\angle(A_i,A_j)-\angle(B_i,B_j)| \quad (4)$$

In these expressions, n corresponds to the lower of cluster A or B's coordination numbers, A_{ix} is the x coordinate position of atom i in cluster A (with corresponding definitions for y and z coordinates), m is the number of bonds in cluster A, and $\angle(A_i,A_j)$ calculates the angle

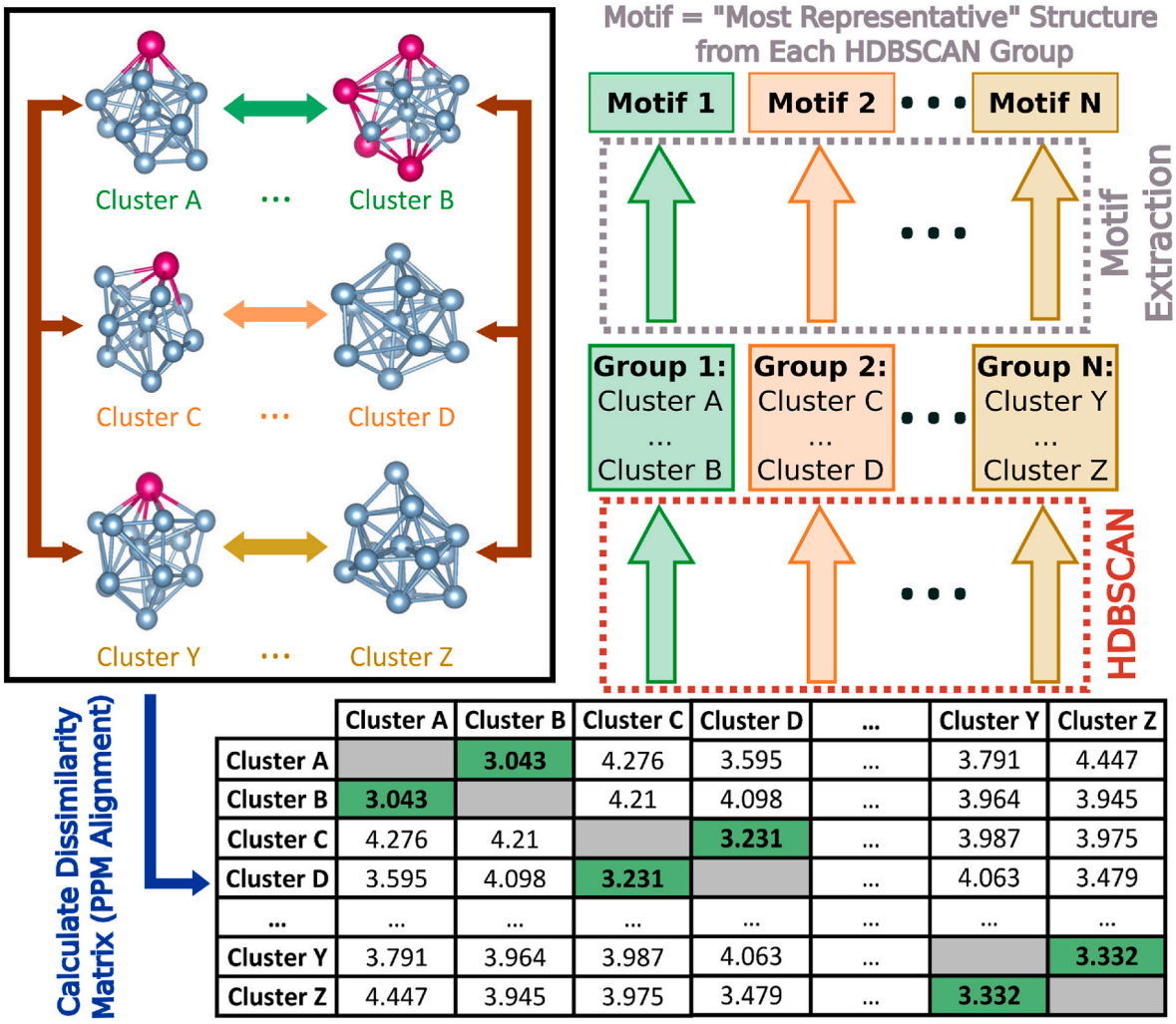

	Cluster A	Cluster B	Cluster C	Cluster D	...	Cluster Y	Cluster Z
Cluster A		3.043	4.276	3.595	...	3.791	4.447
Cluster B	3.043		4.21	4.098	...	3.964	3.945
Cluster C	4.276	4.21		3.231	...	3.987	3.975
Cluster D	3.595	4.098	3.231		...	4.063	3.479
...	...	...	...	...	...	...	...
Cluster Y	3.791	3.964	3.987	4.063	...		3.332
Cluster Z	4.447	3.945	3.975	3.479	...	3.332	

Fig. 1. Illustration of the PPM alignment and HDBSCAN process for sample local atomic structures of an Al–Sm simulated liquid at 1000K. Note that the structures with a lower dissimilarity relative to one another are placed into the same HDBSCAN group. Following this grouping step, we extract a representative motif from each HDBSCAN group as the structure with the lowest average dissimilarity to the other members. These representative motifs can then be compared.

between atoms i and j through the central atom of the cluster. The geometric average of these parameters can then be used to calculate a dissimilarity value (D) for the two clusters:

$$D = \sqrt[4]{L^2 \times L^1 \times L^\infty \times L^4} \quad (5)$$

A large D value indicates low similarity between clusters A and B. When this analysis is performed on all binary combinations of C clusters, the result is a C x C matrix of dissimilarity values. The HDBSCAN algorithm [95] is then used to group together clusters that are "similar enough" to one another, based on the calculated dissimilarity values. This process is summarized in Fig. 1, which illustrates the PPM alignment and HDBSCAN process for sample clusters from an Al–Sm simulated liquid. In this figure, the clusters are all compared to one another, and those that are most similar to one another are placed into the same HDBSCAN group. Using the dissimilarity values between the clusters in each HDBSCAN group, we can also extract a representative "motif" structure that has the lowest average dissimilarity to all other clusters in the group.

The most computationally intensive part of this analysis is the alignment of the ~30,000 binary combinations of clusters in each simulated liquid structure. To address this, we divided the clusters into ~30 subsets each including 1000 randomly selected clusters until fewer than 1000 clusters remain, at which point the remainder are placed into a final smaller subset. (Fig. 2a–b). The analysis described above was then performed on each of the subsets; PPM alignment was performed to obtain a dissimilarity matrix local to the clusters within a given subset (Fig. 2c), HDBSCAN was performed to place the clusters into groups that were similar to one another, and the representative motif from each HDBSCAN group was extracted (Fig. 2d). Next, *the representative motifs* from each of the subsets were recombined to form a single super-set of clusters. These motifs were aligned (PPM) and assigned to super-groups (HDBSCAN) based on their similarities (Fig. 2e). Because we have a record of the original clusters that each of these motifs represent, we can then replace the representative motifs in each super-group with the corresponding original clusters from all of the subsets (Fig. 2f), thus enabling the comparison of clusters across subsets. This "split/recombine" method compared favorably with an "all-to-all" comparison of a 10,000-cluster structure, as described in Appendix A.

After structural analysis, either by Voronoi tessellation or the HDBSCAN grouping method described above, the measure of *order* in the liquid was quantified using the mathematical variance of the distribution of clusters making up the overall structure [47]:

$$\sigma^2 = \frac{\sum_{i=1}^{G}(X_i - \mu)^2}{G} \quad (6)$$

In Eq.(6), σ^2 is the variance, and X, μ, and G correspond to the contribution of cluster type i to the overall distribution, the distribution mean, and the number of terms (cluster groups) in the distribution, respectively, and the summation in the numerator corresponds to the summation across all cluster types. In the case of Voronoi tessellation, we calculated the variance from the fraction of the system associated with each set of observed Voronoi indices. Error bars for the Voronoi variance results were determined from the standard deviation of this calculation on four equilibrated liquid structures. For the HDBSCAN method, the variance was calculated from the fraction of the clusters associated with each of the HDBSCAN super-groups. See Appendix B for explanation of the error bar determination for the HDBSCAN variance.

3. Results

After calculating the variance of both the Voronoi and HDBSCAN cluster populations in the liquid for compositions in the investigated systems, we arrive at the results presented in Fig. 3 for the Cu–Zr and Ni–Nb systems, Fig. 4 for the Al–Sm and Au–Si systems, and Fig. 5 for the Al–Ni–Zr system. For comparison with the variance data for the simulated liquid structures, shaded regions in Figs. 3 and 4 correspond to experimental glass forming compositions and the vertical lines denote local maxima in the experimental glass-forming ability (e.g. critical casting thickness). The experimental glass-forming regions for the ternary system in Fig. 5 are shown on the figure by red/yellow outlines and a red dot. Note that the Voronoi and HDBSCAN variance results are on different y-axis scales for the binary systems given the drastic difference in the magnitude of the two metrics; the HDBSCAN variance is always four or more orders of magnitude larger than the Voronoi variance. This is due to the vastly different number of cluster groups (G) considered in Eq. (6) for the two methods. For the Voronoi technique, considering every set of Voronoi indices observed in the liquid structure results in approximately 6000 groups, most of which contribute only a very small fraction to the overall structure. Indeed, the Voronoi analysis typically resulted in the largest group containing approximately 3–4% of the atoms in the system. In contrast, only 6–8 HDBSCAN groups are needed to characterize all clusters in the liquid structure, and the most common groups contain approximately 25–35% of all atoms.

The Cu–Zr system (Fig. 3a) is one of the most heavily-studied binary glass-forming systems, with glass formation observed over a wide range from $Cu_{46}Zr_{54}$–$Cu_{68}Zr_{32}$ [70] and local maxima in the critical casting thickness of glass-formers reported at $Cu_{50}Zr_{50}$, $Cu_{56}Zr_{44}$ and $Cu_{64}Zr_{36}$ [69–75]. Investigating Fig. 3a, we can see that the Voronoi variance does not exhibit much variation over this range. While the extreme

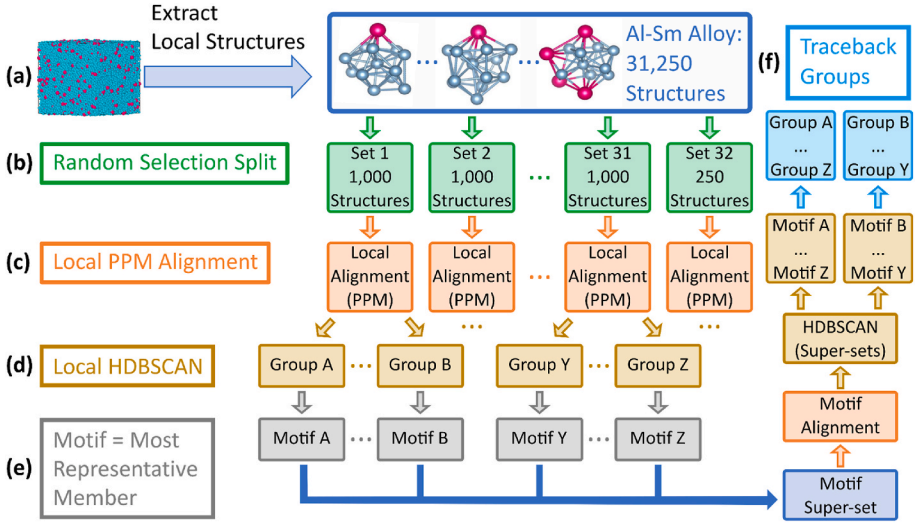

Fig. 2. Flowchart of the "Split/Recombine" approach used to reduce the number of necessary comparisons for point-pattern matching. (a) Local nearest neighbor atomic structures are extracted from the simulation cell and (b) randomly split into sets of 1000 structures with the final set containing the sub-1000 atom remainder of the system. (c) PPM alignment within each of these smaller groups generates the dissimilarity matrix, which is used by the HDBSCAN algorithm in (d) to yield groups with similar structures within each of the 1000 atom sets. (e) Representative "motifs" with the highest degree of similarity to all of the structures within the HDBSCAN group are then selected. (f) These motifs are combined, and PPM alignment and HDBSCAN analysis are applied to obtain the HDBSCAN groups for the entire structure. From these final groups, the motifs can be traced back to all of the local atomic structures that each one represents.

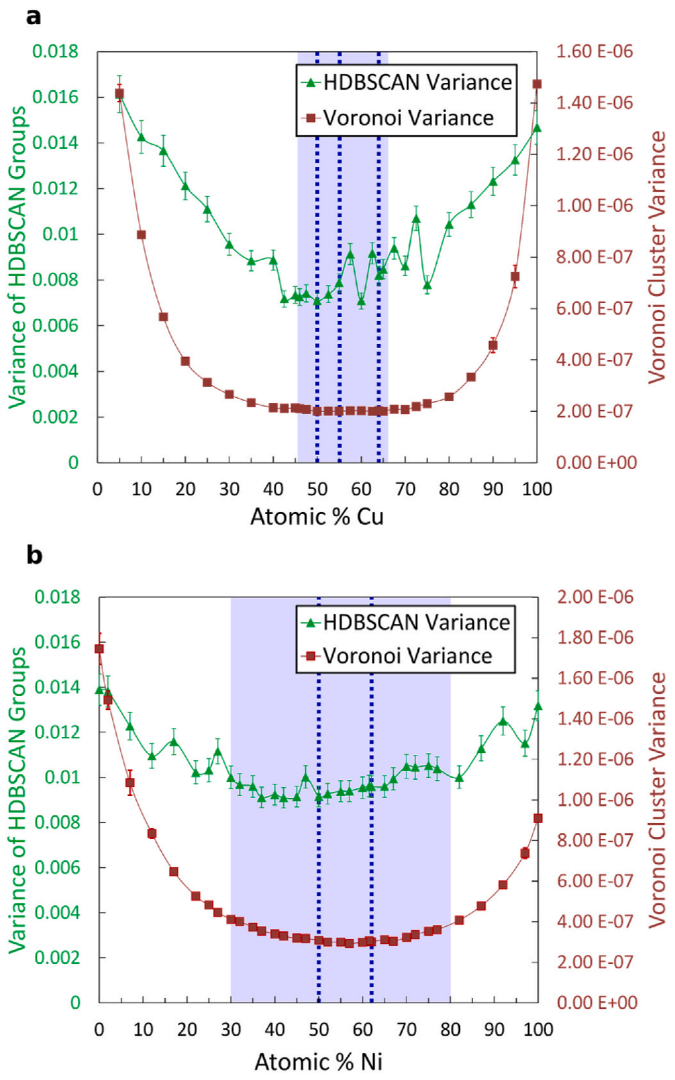

Fig. 3. (a) HDBSCAN variance (green) and Voronoi variance (red) calculated for the simulated Cu–Zr liquid structure at 1450 K as a function of composition. (b) HDBSCAN variance (green) and Voronoi variance (red) calculated for the simulated Ni–Nb liquid structure at 2300 K as a function of composition. The shaded regions in both plots denote the reported experimental glass-forming ranges [70,76,79] while the vertical dashed lines represent discrete local maxima in GFA. (For interpretation of the references to color in this figure legend, the reader is referred to the Web version of this article.)

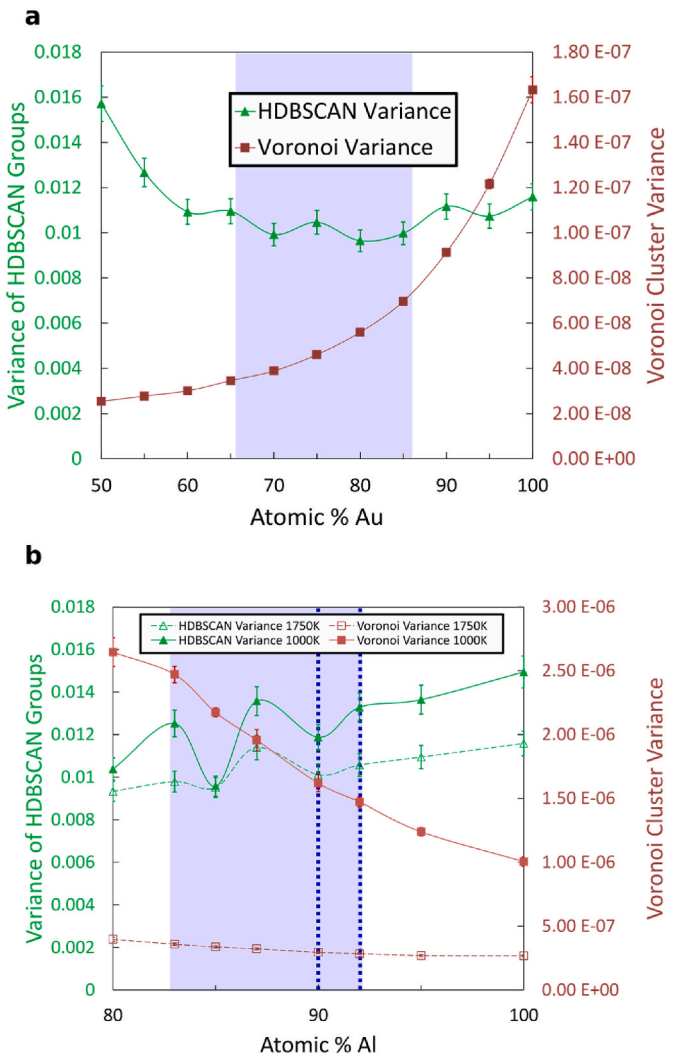

Fig. 4. (a) HDBSCAN variance (green) and Voronoi variance (red) calculated for the simulated Au–Si liquid structure at 1760K as a function of composition. (b) HDBSCAN variance (green) and Voronoi variance (red) calculated for the simulated Al–Sm liquid structures at 1000K (solid line) and 1750K (dashed line) as a function of composition. Shaded regions denote reported experimental glass-forming regimes [4,81,85,86] while vertical dashed lines in (b) denote compositions with reportedly higher GFA [66,82–84]. (For interpretation of the references to color in this figure legend, the reader is referred to the Web version of this article.)

compositions have much larger variance values, there is a wide, flat minimum in this parameter between $Cu_{20}Zr_{80}$ and $Cu_{80}Zr_{20}$. On the other hand, the HDBSCAN variance exhibits much more variation in this same regime. Moreover, the compositions with the lowest values for this measurement line up extremely well with the range of experimental glass-formers in this system (shaded in Fig. 3a).

The Ni–Nb system (Fig. 3b) is another known glass-forming system with high-GFA alloys occurring at $Ni_{62}Nb_{38}$ [78] and $Ni_{50}Nb_{50}$ [77]. While marginal glass-formers have been identified in the range of $Ni_{30}Nb_{70}$–$Ni_{80}Nb_{20}$, these compositions were synthesized by vapor deposition, suggesting comparatively high critical cooling rates [76,79]. As seen in the Cu–Zr alloys, one observes a general lack of topography in the Voronoi variance, while the lowest HDBSCAN variance values in the Ni–Nb system occur at $Ni_{30}Nb_{70}$–$Ni_{45}Nb_{55}$ and $Ni_{50}Nb_{50}$–$Ni_{67}Nb_{33}$. The latter region lines up well with the best experimentally reported glass-formers and the former lies within the reported range of vapor-deposited glasses with marginal GFA.

Both Cu–Zr and Ni–Nb are bulk glass-formers, meaning that they exhibit high GFA relative to other binary systems. To test more marginal glass-forming systems, particularly those including non-transition metals, we considered Al–Sm and Au–Si alloys. In Fig. 4a, the HDBSCAN variance is relatively flat over the range $Au_{60}Si_{40}$–$Au_{95}Si_5$, although the lowest Au–Si HDBSCAN variance values ($Au_{70}Si_{30}$–$Au_{85}Si_{15}$) overlap well with the experimentally reported glass-formers ($Au_{66}Si_{34}$–$Au_{86}Si_{14}$ [4,86]). In contrast, the Voronoi variance increases monotonically with increasing Au across the range of study. In Fig. 4b, the HDBSCAN variance exhibits three local minima at $Al_{80}Sm_{20}$, $Al_{85}Sm_{15}$, and $Al_{90}Sm_{10}$; one of these ($Al_{90}Sm_{10}$) lines up with two local maxima in experimental GFA that have been discussed in the literature at $Al_{90}Sm_{10}$ and $Al_{92}Sm_8$ [66,82–84], while $Al_{85}Sm_{15}$ falls within the full range of experimentally observed glass-formers ($Al_{83}Sm_{17}$–$Al_{92}Sm_8$ [66, 80–85]). Although the correlation between experimental GFA and the HDBSCAN variance is less clearly defined in this system, the Voronoi variance again shows no correlation, decreasing monotonically with increasing Al content.

The ternary Al–Ni–Zr system serves as a test-case to see how well the

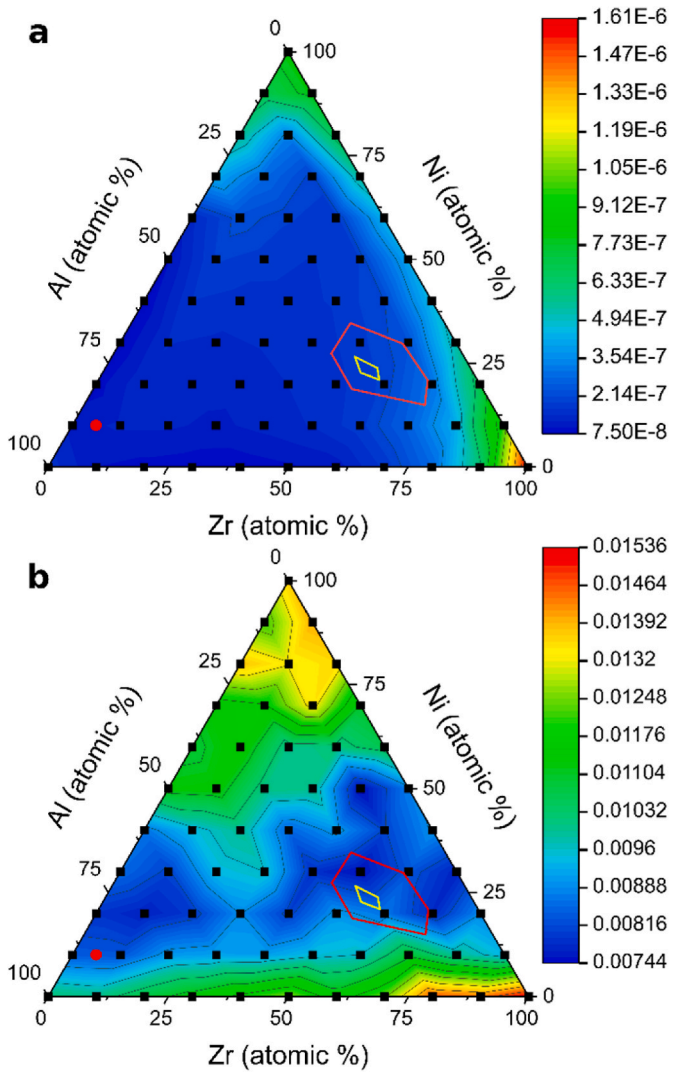

Fig. 5. (a) Voronoi variance and (b) HDBSCAN variance ternary plots for simulated Al–Ni–Zr liquid structures at 1800K. In each, color scales represent the variance values and the black squares denote the investigated compositions. Experimentally-observed glass-forming compositions are denoted by the red outline (Zr-rich corner [47]) and red dot (Al-rich corner [87]). The yellow outline within the red-outlined region denotes the "best" glass forming compositions identified by the high-throughput synthesis technique employed by Wang et al. [47]. (For interpretation of the references to color in this figure legend, the reader is referred to the Web version of this article.)

variance parameter scales into higher-order systems as a predictor of GFA. More than 100 compositions were simulated this system, denoted by the black squares on the ternary diagrams of Fig. 5. Multiple experimental glass-formers have been reported in this system. Wang et al. used a high-throughput combinatorial approach to experimentally identify Zr-rich glass-forming compositions [47]. The full range of synthesized glasses in this region is outlined in red, while those with the highest GFA observed by this combinatorial method are outlined in yellow. A melt spun glass-former at $Al_{85}Ni_{10}Zr_5$ has also been reported and is denoted in Fig. 5 by a red dot [87]. As in the binary systems discussed above, the Voronoi variance (Fig. 5a) shows very little topography and no correlation with the positions of the experimental glass-formers. In contrast, the HDBSCAN variance (Fig. 5b) exhibits very good correlation between the low variance compositions (blue) and the experimental glass-formers. Note the difference in scalebars between the plots, as the range of observed HDBSCAN variance (Fig. 5a) is more than three orders of magnitude larger than that of the Voronoi variance (Fig. 5b).

4. Discussion

4.1. Structural variance in the liquid and glass-forming ability

The first goal of this work is to develop a high-throughput computational method to identify potential metallic glass-forming compositions within a given alloy family. We do so by analyzing the high temperature liquid structure, rather than the simulated glass structure, because this eliminates the need for more time- and resource-intensive quenching and equilibration at lower temperatures. Furthermore, due to the rapid equilibration observed in the liquid state, the simulated liquid structures are more likely to be representative of "real", experimental liquid structures. Simulated glass structures, on the other hand, intrinsically require longer equilibration times, making the simulation of structures that are comparable to experimentally observed glasses extremely time-consuming.

Wang et al. previously proposed that the variance of the Voronoi cluster population in the liquid should be inversely correlated to GFA in metallic alloys [47]. The premise of this argument is that higher variance means that the majority of the structure can be described by a narrow distribution of characteristic structural elements (i.e. atomic clusters), while low variance implies that many different structural elements contribute equally to describe the system. That is, the variance parameter calculated for a liquid structure directly correlates with the degree of structural order in the liquid state. As proposed by Wang et al., an alloy with higher order in the liquid should lead to easy crystallization and poor GFA and vice versa, leading to the proposed inverse relationship between variance and GFA in metallic alloys [47]. While Wang et al. demonstrated this basic premise for several (related) ternary glass forming systems, questions have recently been raised about the ability of Voronoi indices to effectively compare and differentiate among unique local geometric arrangements. Notably, to improve the ability to differentiate among compositions, Wang et al. only considered the five most common Voronoi clusters in the structure in their variance calculation; this implies that approximately 90% of the atoms were not considered in the analysis. This leads to the current research comparing Voronoi tessellation [47] with the PPM/HDBSCAN [53,54] technique.

We compare the variance results obtained using these two clustering methods to known experimental glass-forming compositions in the five examined systems in Figs. 3–5. For the Cu–Zr system (Fig. 3a), the experimental glass forming compositions occur in the ranges where both the HDBSCAN and Voronoi variances exhibit minima. However, the HDBSCAN minimum is much narrower, and the alignment with the regions of high GFA is quite striking. Using a high-throughput synthesis and characterization strategy, Tsai and Flores [69] identified two continuous glass forming ranges in Cu–Zr, centered around $Cu_{64.7}Zr_{35.3}$ and $Cu_{50.2}Zr_{49.8}$. While we remain cautious about over-interpreting small variations in the simulation results presented here, it is notable that these compositional regions are separated by local peaks in the HDBSCAN variance, suggesting that structural differences in the liquid may contribute to the formation of two different glass structures. While these results are consistent with the hypothesis that a minimum in the liquid structure variance may provide an effective screening parameter for GFA, we also note that it is not a sufficient condition, since the local minima at $Cu_{70}Zr_{30}$, and $Cu_{75}Zr_{25}$ do not correlate with known bulk glass-formers. Furthermore, it is unclear how the relative depths of the minima correlate with GFA; $Cu_{64}Zr_{36}$ is known to have the overall largest critical casting thickness [69,70,73,75] and thus highest GFA in this system, but it does not have the lowest variance in the present work. The variance parameter only considers SRO and does not account for the potential higher-order effects of nucleation kinetics and the formation of disordered networks (e.g. MRO) on suppressing diffusion and crystallization. However, the current results suggest that the HDBSCAN variance is an effective first-order screening tool for GFA.

Similar to the Cu–Zr system, in the Ni–Nb system (Fig. 3b), we again observe that both the Voronoi and HDBSCAN approaches result in minima that overlap with the experimentally observed glass forming compositions. The minimum in the Voronoi variance is flat and relatively broad and, while both the Voronoi and HDBSCAN variances line up with the region of vapor-deposited glasses, the HDBSCAN variance again exhibits a narrower minimum range near the best glass-formers in the system ($Ni_{50}Nb_{50}$ and $Ni_{62}Nb_{38}$).

In the first marginal glass-forming system, the Au–Si system shows similarly good agreement between the HDBSCAN variance and experimentally observed glass formation. Interestingly, the Voronoi variance shows no correlation with GFA within the range where the potentials were applicable; indeed, the trends in the HDBSCAN and Voronoi variances with composition are completely different. This is discussed in more detail in Section 4.2.

In the Al–Sm system, the liquid structure was analyzed at 1000 K and 1750 K (Fig. 4b) due to the rapidly decreasing liquidus temperature as one approaches pure Al. While there is less variability with composition in both the Voronoi and HDBSCAN variance parameters at the higher temperature, the general trends at 1000 K and 1750 K are the same. As in the Au–Si system, the Voronoi variance of the Al–Sm alloys shows no correlation with GFA, reaching a minimum at 100 at% Al, which is known to crystallize readily. In contrast, the HDBSCAN variance reaches a maximum at 100 at% Al, and there are local minima which line up well with the end regions of the experimental glass-forming regime, in particular the most studied glass former in this system, $Al_{90}Sm_{10}$. It is notable that the HDBSCAN variance appears to drop at $Al_{80}Sm_{20}$, where glass forming has not been reported, and rise at $Al_{87}Sm_{13}$, which is within the experimental glass-forming region. With respect to $Al_{80}Sm_{20}$, a recent publication has shown that the atomic diffusivity at this composition does not deviate significantly from linearity as a function of temperature, suggesting that the composition may have marginal GFA [98]. Additional studies of the thermodynamics of the high-temperature intermetallic phase near this composition ($Al_{11}Sm_3$) [99,100] suggest a complex competition between various metastable and equilibrium structures as a function of temperature, likely contributing to the low variance. These results suggest that a more detailed experimental study of glass forming ability as a function of composition in this system may be warranted.

We have extended this analysis to the ternary Al–Ni–Zr system (Fig. 5). While Wang et al. [47] showed similar results for Voronoi variance of Al–Ni–Zr liquids, the plot presented here (Fig. 5a) is markedly different due to the inclusion of all Voronoi indices in the calculation rather than limiting the calculation to a small subset of most common Voronoi indices, as was done in Wang et al.'s original work. Taking all Voronoi clusters into account, the Voronoi variance shows very little topography and no correlation to the experimental glass-formers in the system. In contrast, the HDBSCAN variance has the second lowest value of any investigated composition at $Al_{20}Ni_{30}Zr_{50}$, in excellent agreement with Wang et al.'s best experimental glass former at $Al_{21.4}Ni_{23.9}Zr_{54.7}$ [47] while the third lowest value falls at $Al_{70}Ni_{20}Zr_{10}$, which also has been identified experimentally as an Al-rich glass former [87]. (The experimental GFA for the composition with the lowest HDBSCAN variance, $Al_{10}Ni_{40}Zr_{50}$, has not been reported.) These results suggest that the validity of this screening technique scales well to higher-order systems.

4.2. Comparison of HDBSCAN and voronoi cluster populations

The discussion above suggests that there is an inverse correlation between the HDBSCAN variance and experimental glass-forming ability within a given system, while the Voronoi method provides much less specificity for the Cu–Zr, Ni–Nb, and Al–Ni–Zr systems and is completely insufficient for describing GFA in the Au–Si and Al–Sm systems. To understand why these methods produce different results, we now compare how the two analyses divide the liquid structures into characteristic clusters. For simplicity, we focus on the binary systems.

Voronoi tessellation constructs a three-dimensional proximity map that isolates the volume that is closer to a given atom than to any other atom in the simulation cell. Once these volumes are determined, a set of Voronoi indices are used to characterize the number of faces with 3, 4, 5, or 6 vertices on the polyhedron that best represents the shape of this volume, with the combined volume of all polyhedra intrinsically adding up to 100% of the simulated volume. Polyhedra with the same indices are grouped together when calculating the variance of the cluster distribution, while those with different indices are often assumed to be structurally distinct. However, recent work [53] showing that the geometry of clusters with the same set of Voronoi indices can be quite dissimilar to one another, while those with different indices can have high geometric similarity, suggests that categorizing the clusters based on the Voronoi indices alone may be an inadequate description of the SRO. Furthermore, grouping based on Voronoi indices results in a large number of "distinct" cluster types with minimal contribution to the overall cluster population, such that small but potentially meaningful changes in the structure with composition are likely to be washed out by the generally broad population distribution of clusters.

In contrast to Voronoi tessellation, the PPM technique uses the geometric properties of the local (nearest neighbor) atomic structures to determine a numeric dissimilarity between any binary combination of clusters. HDBSCAN then creates groups of clusters that are "similar enough to be considered the same", without requiring them to have identical features, and which can be visualized using a representative motif. This analysis results in only 6–8 representative motifs which account for 96–99% of all atoms in the system. Unlike Voronoi tessellation, the volumes contained by the resultant HDBSCAN groups do not necessarily add up to 100% of the simulated volume because HDBSCAN can classify particular local structures as outliers that do not belong to any group, removing them from further consideration in the variance calculation. The smaller total number of motifs (i.e. smaller G value in Eq. (6)) results in larger variance values for the cluster population distributions, which in turn are more sensitive to structural changes associated with composition.

By tracing each atom in the structure to both its Voronoi and HDBSCAN groups, we can directly compare how the two analyses represent the overall liquid structure. Fig. 6 (Cu–Zr and Ni–Nb) and Fig. 7 (Au–Si and Al–Sm at 1000 K) illustrate how the atoms belonging to each of the twenty-five most common sets of Voronoi indices in a given liquid are divided among the HDBSCAN groups. For each alloy family, an example of a glass forming composition (right) is compared with a non-glass former (left); similar results were obtained for other compositions. Note that the plots present the fraction of atoms with each set of indices corresponding to each of the HDBSCAN groups for that composition. The sets of Voronoi indices are grouped by coordination number (CN), which is given by the sum of the four indices in each set. Finally, the rightmost series on each plot provides the overall HDBSCAN group fractions for the entire liquid structure.

Regardless of composition or alloy system, we first observe that local atomic arrangements described by the same Voronoi indices are always split into several HDBSCAN groups, suggesting that Voronoi indices are poor descriptors of atomic cluster geometry. This is consistent with prior work by Maldonis et al., who showed that polyhedra with the same Voronoi indices could exhibit a high dissimilarity D (Eq. (5)) [54]. Recall that Voronoi tessellation is based on the atoms' relative proximity to each other and the shape of volume closest to a given atom, and provides no direct information about bond lengths or bond angles, which are fundamental features of cluster geometry.

Although the sets of Voronoi indices are split across multiple HDBSCAN groups, in the Cu–Zr and Ni–Nb systems, Voronoi polyhedra with the same coordination number often exhibit similar HDBSCAN group fractions, and these fractions are often significantly enriched or depleted relative to the overall liquid structure (rightmost series). For example, in Cu_5Zr_{95} (Fig. 5a1), most of the Voronoi clusters with CN 12

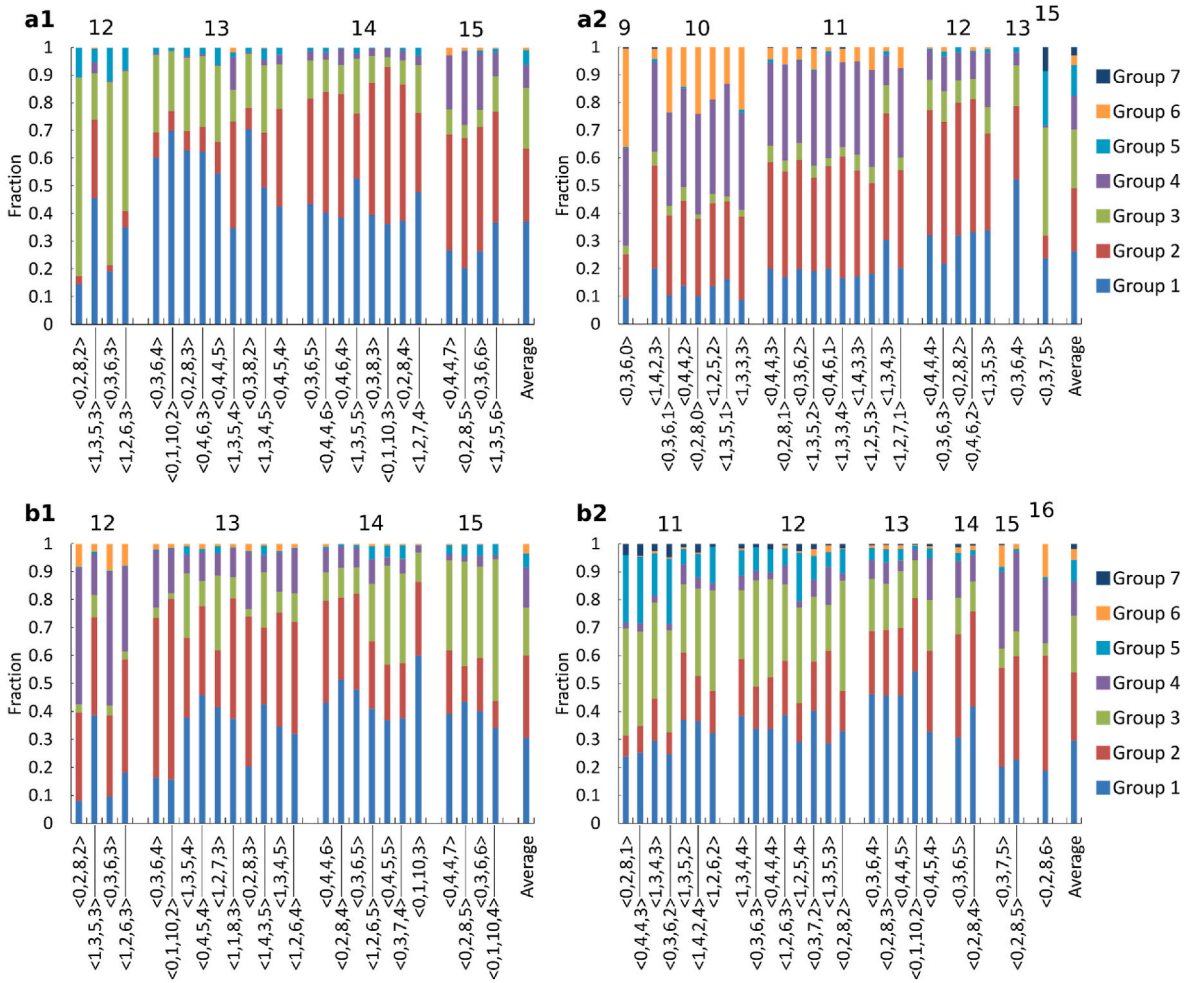

Fig. 6. Distribution of the twenty-five most common sets of Voronoi Indices across HDBSCAN groups for representative non-glass-forming (a1, b1) and glass-forming (a2, b2) compositions in the (a) Cu–Zr and (b) Ni–Nb systems: (**a1**) Cu_5Zr_{95}, (**a2**) $Cu_{45}Zr_{55}$, (**b1**) $Ni_{12}Nb_{88}$, and (**b2**) $Ni_{62}Nb_{38}$. Sets of Voronoi indices are grouped by coordination number as noted across the top of each plot. Note that the rightmost series in each plot corresponds to the HDBSCAN group fractions for the entire liquid structure.

exhibit an overexpression of HDBSCAN Group 3 relative to the average, while in $Cu_{65}Zr_{35}$ (Fig. 6a2), Group 2 is overexpressed in CN 11 and 12. Similar variations in the HDBSCAN group fractions with coordination number are observed for Ni–Nb (Fig. 6b alloys). This (mild) sensitivity of the HDBSCAN groupings to coordination number is somewhat surprising since coordination number is only considered in the number of averaged terms in Eqs. (1), (2) and (4), and not in any of the geometric features evaluated by either the PPM alignment or HDBSCAN grouping process.

In contrast, while the local atomic arrangements described by each set of Voronoi indices are again split among several HDBSCAN groups for the Au–Si and Al–Sm systems (Fig. 7), we find that many of the twenty-five most common sets of Voronoi indices exhibit HDBSCAN group fractions quite similar to the overall liquid structure (rightmost series). Little variation in the HDBSCAN group fractions is observed as a function of coordination number. That is, the HDBSCAN groups are not as sensitive to coordination number in these systems.

The relative sensitivity of the HDBSCAN groupings to coordination number for the Cu–Zr and Ni–Nb systems likely explains why the variance in the Voronoi cluster population follows the same general trend with composition as the variance in the HDBSCAN cluster population in these systems. By virtue of their coordination number, some sets of Voronoi indices are coupled with a certain distribution of HDBSCAN groups, and this coupling carries forward into the population distribution and variance of both types of clusters. On the other hand, in Al–Sm and Au–Si, the HDBSCAN cluster population within each set of Voronoi indices is very similar to the average population, so changes in the relative fractions of different Voronoi cluster types do not have significant impact on the population of HDBSCAN clusters, and thus the variance of these populations is decoupled. It is unclear at this time if this decoupling is a result of the inclusion of non-transition metals. Notably, both Sm (trigonal) and Si (diamond cubic) have lower symmetry crystal structures than the other elements studied, which may reduce the atomic packing efficiency in the corresponding binary systems.

5. Conclusion

In this work, we have shown that order in the liquid state is inversely correlated with glass-forming ability across a range of metallic systems including both good (Cu–Zr, Ni–Nb, Al–Ni–Zr) and marginal (Al–Sm, Au–Si) experimental glass-forming systems, where “order” was defined as the mathematical variance of the population distribution of atomic clusters. The data presented here suggests that, rather than being uniformly disordered, the degree of structural disorder of the liquid state varies significantly with composition, giving rise to some compositions which are more likely to vitrify upon quenching. While this analysis does not account for medium-range order and temperature-dependent evolution of structure, the ability to effectively identify experimental glass-forming regimes without consideration of these factors yields a high-

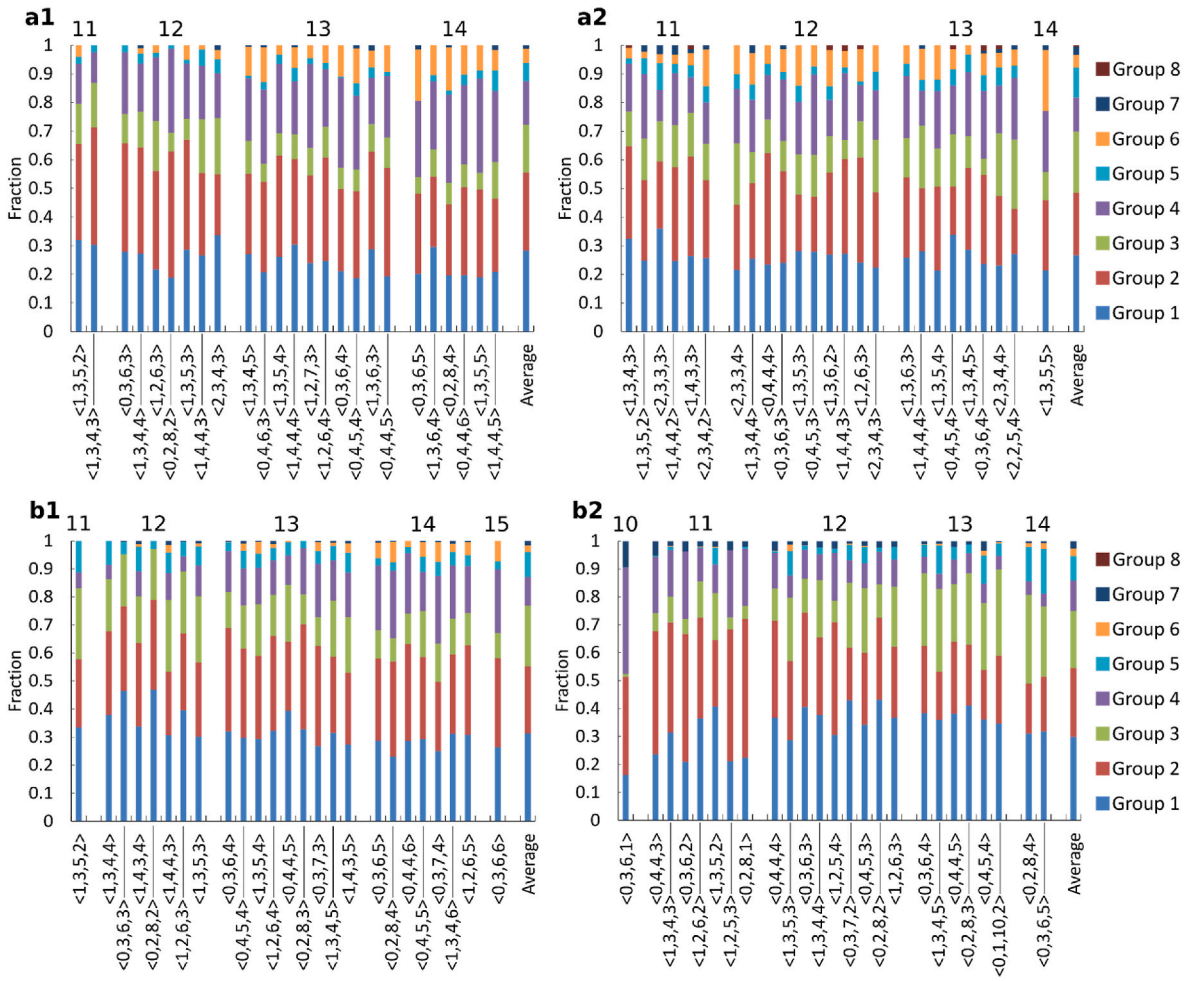

Fig. 7. Distribution of the twenty-five most common sets of Voronoi Indices across HDBSCAN groups for representative non-glass-forming (a1, b1) and glass-forming (a2, b2) compositions in (a) Au–Si and (b) Al–Sm at 1000K: (**a1**) $Au_{100}Si_0$, (**a2**) $Au_{70}Si_{30}$, (**b1**) $Al_{100}Sm_0$, and (**b2**) $Al_{83}Sm_{13}$. Sets of Voronoi indices are grouped by coordination number as noted across the top of each plot. Note that the rightmost series in each plot corresponds to the HDBSCAN group fractions for the entire liquid structure.

throughput technique that could be used as a screening tool for GFA in a wide array of metallic systems. The populations of characteristic atomic clusters were quantified using two techniques: a conventional Voronoi tessellation approach, in which clusters with the same Voronoi indices were grouped together, and a point-pattern matching geometric analysis that enabled grouping via a machine learning-based clustering algorithm (HDBSCAN). Voronoi indices were shown to be poor descriptors of the geometry of local atomic clusters, with atomic environments corresponding to each set of indices being split among multiple HDBSCAN groups. Furthermore, while Voronoi tessellation can produce thousands of polyhedra with independent indices, the same disordered structure can be described by just 6–8 characteristic HDBSCAN motifs. As a result, the PPM/HDBSCAN approach provided much greater specificity in identifying compositions with low cluster population variance and better overlap with the experimental glass-forming regions in both good and marginal glass-forming systems.

Finally, it should be noted that focusing our analyses on the simulated liquid is a more time-efficient approach to studying GFA than examining the quenched structure, since fewer time steps are required to produce a satisfactory structure. Furthermore, in contrast to questions about the similarity between simulated quenched structures and experimental glasses, the simulated liquids are more likely to be representative of the true liquid structure due to the shorter kinetic equilibration times at high temperatures. Therefore, not only is it more time efficient, but this type of simulated liquid analysis also produces more realistic data than could likely be achieved from lower temperature analyses where the kinetic equilibration times are far beyond the timescales of typical MD simulations.

Author statement

Porter Weeks: Data Curation, Formal Analysis, Investigation, Methodology, Validation, Visualization, Writing-original draft, Writing-review and editing **Katharine Flores:** Funding Acquisition, Project Administration, Supervision, Writing-original draft, Writing-review and editing.

Declaration of competing interest

The authors declare that they have no known competing financial interests or personal relationships that could have appeared to influence the work reported in this paper.

Acknowledgements

This work was supported by the National Science Foundation under Grant No. DMR-2004630. MD simulations and subsequent analyses were performed using the Washington University Center for High Performance Computing, which is partially supported through NIH grant S10 OD018091.

Appendix A. Supplementary data

Supplementary data to this article can be found online at https://doi.org/10.1016/j.intermet.2022.107560.

References

[1] A. Inoue, N. Nishiyama, H. Kimura, Preparation and thermal stability of bulk amorphous Pd 40 Cu 30 Ni 10 P 20 alloy cylinder of 72 mm in diameter, Mater. Trans., JIM 38 (1997) 179–183, https://doi.org/10.2320/matertrans1989.38.179.

[2] A. Inoue, H. Yamaguchi, T. Zhang, T. Masumoto, Al-La-Cu amorphous alloys with a wide supercooled liquid region, Mater. Trans., JIM 31 (1990) 104–109, https://doi.org/10.2320/matertrans1989.31.104.

[3] A. Peker, W.L. Johnson, A highly processable metallic glass: Zr41.2Ti 13.8Cu12.5Ni10.0Be22.5, Appl. Phys. Lett. 63 (1993) 2342–2344, https://doi.org/10.1063/1.110520.

[4] W. Klement, R.H. Willens, P. Duwez, Non-crystalline structure in solidified Gold-Silicon alloys, Nature 187 (1960) 869–870, https://doi.org/10.1038/187869b0.

[5] C.A. Schuh, T.C. Hufnagel, U. Ramamurty, Mechanical behavior of amorphous alloys, Acta Mater. 55 (2007) 4067–4109, https://doi.org/10.1016/j.actamat.2007.01.052.

[6] J. Schroers, Processing of bulk metallic glass, Adv. Mater. 22 (2010) 1566–1597, https://doi.org/10.1002/adma.200902776.

[7] D. Turnbull, Under what conditions can A glass Be formed? Contemp. Phys. 10 (1969) 473–488, https://doi.org/10.1080/00107516908204405.

[8] A. Inoue, W. Zhang, T. Zhang, K. Kurosaka, High-strength Cu-based bulk glassy alloys in Cu-Zr-Ti and Cu-Hf-Ti ternary systems, Acta Mater. 49 (2001) 2645–2652, https://doi.org/10.1016/S1359-6454(01)00181-1.

[9] Z. Long, G. Xie, H. Wei, X. Su, J. Peng, P. Zhang, A. Inoue, On the new criterion to assess the glass-forming ability of metallic alloys, Mater. Sci. Eng. 509 (2009) 23–30, https://doi.org/10.1016/j.msea.2009.01.063.

[10] T.D. Shen, Y. He, R.B. Schwarz, Bulk amorphous Pd-Ni-Fe-P alloys: preparation and characterization, J. Mater. Res. 14 (1999) 2107–2115, https://doi.org/10.1557/JMR.1999.0285.

[11] T.A. Waniuk, J. Schroers, W.L. Johnson, Critical cooling rate and thermal stability of Zr-Ti-Cu-Ni-Be alloys, Appl. Phys. Lett. 78 (2001) 1213–1215, https://doi.org/10.1063/1.1350624.

[12] Z.P. Lu, C.T. Liu, A new glass-forming ability criterion for bulk metallic glasses, Acta Mater. 50 (2002) 3501–3512, https://doi.org/10.1016/S1359-6454(02)00166-0.

[13] Y. Li, Formation, structure and properties of bulk metallic glasses, J. Mater. Sci. Technol. 15 (1999) 97–110.

[14] J.D. Bernal, J. Mason, Packing of spheres: Co-ordination of randomly packed spheres, Nature 188 (1960) 910–911, https://doi.org/10.1038/188910a0.

[15] J.D. Bernal, Geometry of the structure of monatomic liquids, Nature 185 (1960) 68–70.

[16] P.H. Gaskell, A new structural model for amorphous transition metal silicides, borides, phosphides and carbides, J. Non-Cryst. Solids 32 (1979) 207–224, https://doi.org/10.1016/0022-3093(79)90073-5.

[17] D.B. Miracle, A structural model for metallic glasses, Nat. Mater. 3 (2004) 697–702, https://doi.org/10.1038/nmat1219.

[18] D.B. Miracle, The efficient cluster packing model - an atomic structural model for metallic glasses, Acta Mater. 54 (2006) 4317–4336, https://doi.org/10.1016/j.actamat.2006.06.002.

[19] K.J. Laws, D.B. Miracle, M. Ferry, A predictive structural model for bulk metallic glasses, Nat. Commun. 6 (2015), https://doi.org/10.1038/ncomms9123.

[20] I. Kaban, P. Jóvári, V. Kokotin, O. Shuleshova, B. Beuneu, K. Saksl, N. Mattern, J. Eckert, A.L. Greer, Local atomic arrangements and their topology in Ni–Zr and Cu–Zr glassy and crystalline alloys, Acta Mater. 61 (2013) 2509–2520, https://doi.org/10.1016/j.actamat.2013.01.027.

[21] J.L. Finney, Modelling the structures of amorphous metals and alloys, Nature 266 (1977) 309–314, https://doi.org/10.1038/266309a0.

[22] N.A. Mauro, M. Blodgett, M.L. Johnson, A.J. Vogt, K.F. Kelton, A structural signature of liquid fragility, Nat. Commun. 5 (2014), https://doi.org/10.1038/ncomms5616.

[23] K.F. Kelton, G.W. Lee, A.K. Gangopadhyay, R.W. Hyers, T.J. Rathz, J.R. Rogers, M.B. Robinson, D.S. Robinson, First X-ray scattering studies on electrostatically levitated metallic liquids: demonstrated influence of local icosahedral order on the nucleation barrier, Phys. Rev. Lett. 90 (2003) 4, https://doi.org/10.1103/PhysRevLett.90.195504.

[24] R. Dai, R. Ashcraft, K.F. Kelton, A possible structural signature of the onset of cooperativity in metallic liquids, J. Chem. Phys. 148 (2018) 204502, https://doi.org/10.1063/1.5026801.

[25] R. Dai, J.C. Neuefeind, D.G. Quirinale, K.F. Kelton, X-ray and neutron scattering measurements of ordering in a Cu 46 Zr 54 liquid, J. Chem. Phys. 152 (2020) 164503, https://doi.org/10.1063/5.0003816.

[26] N.A. Mauro, V. Wessels, J.C. Bendert, S. Klein, A.K. Gangopadhyay, M.J. Kramer, S.G. Hao, G.E. Rustan, A. Kreyssig, A.I. Goldman, K.F. Kelton, Short- and medium-range order in Zr80Pt20 liquids, Phys. Rev. B Condens. Matter 83 (2011) 184109, https://doi.org/10.1103/PhysRevB.83.184109.

[27] M.L. Johnson, N.A. Mauro, A.J. Vogt, M.E. Blodgett, C. Pueblo, K.F. Kelton, Structural evolution and thermophysical properties of ZrxNi100 − x metallic liquids and glasses, J. Non-Cryst. Solids 405 (2014) 211–218, https://doi.org/10.1016/J.JNONCRYSOL.2014.10.026.

[28] P.J. Steinhardt, D.R. Nelson, M. Ronchetti, Icosahedral bond orientational order in supercooled liquids, Phys. Rev. Lett. 47 (1981) 1297, https://doi.org/10.1103/PhysRevLett.47.1297.

[29] V.N. Ryzhov, Local structure and bond orientational order in a Lennard-Jones liquid, J. Phys. Condens. Matter 2 (1990) 5855, https://doi.org/10.1088/0953-8984/2/26/023.

[30] C. Kuiying, L. Hongbo, H. Zhuangqi, Local orientational order in binary liquid Li-In alloys, J. Phys. Condens. Matter 7 (1995) 517, https://doi.org/10.1088/0953-8984/7/3/007.

[31] H. Tanaka, Bond orientational ordering in a metastable supercooled liquid: a shadow of crystallizationand liquid–liquid transition, J. Stat. Mech. Theor. Exp. 2010 (2010) P12001, https://doi.org/10.1088/1742-5468/2010/12/P12001.

[32] H. Tanaka, Roles of bond orientational ordering in glass transition and crystallization, J. Phys. Condens. Matter 23 (2011) 284115, https://doi.org/10.1088/0953-8984/23/28/284115.

[33] H. Tanaka, Bond orientational order in liquids: towards a unified description of water-like anomalies, liquid-liquid transition, glass transition, and crystallization, Eur. Phys. J. E 3510 (2012) (2012) 1–84, https://doi.org/10.1140/EPJE/I2012-12113-Y, 35.

[34] S. Capponi, S. Napolitano, M. Wübbenhorst, Supercooled liquids with enhanced orientational order, Nat. Commun. 31 (2012) (2012) 1–7, https://doi.org/10.1038/ncomms2228, 3.

[35] T.T. Debela, X.D. Wang, Q.P. Cao, Y.H. Lu, D.X. Zhang, H.-J. Fecht, H. Tanaka, J. Z. Jiang, Nucleation driven by orientational order in supercooled niobium as seen via *ab initio* molecular dynamics, Phys. Rev. B 89 (2014) 104205, https://doi.org/10.1103/PhysRevB.89.104205.

[36] W. Xu, M.T. Sandor, Y. Yu, H.B. Ke, H.P. Zhang, M.Z. Li, W.H. Wang, L. Liu, Y. Wu, Evidence of liquid-liquid transition in glass-forming La50Al35Ni15 melt above liquidus temperature, Nat. Commun. 6 (2015) 1–9, https://doi.org/10.1038/ncomms8696.

[37] J.D. Honeycutt, H.C. Andersen, Small system size artifacts in the molecular dynamics simulation of homogeneous crystal nucleation in supercooled atomic liquids, J. Phys. Chem. 90 (1986) 1585.

[38] N. Jakse, A. Pasturel, Local order of liquid and supercooled zirconium by *ab initio* molecular dynamics, Phys. Rev. Lett. 91 (2003) 195501, https://doi.org/10.1103/PhysRevLett.91.195501.

[39] N. Jakse, A. Pasturel, Local order and dynamic properties of liquid and undercooled Cu xZr1-x alloys by ab initio molecular dynamics, Phys. Rev. B Condens. Matter 78 (2008) 214204, https://doi.org/10.1103/PhysRevB.78.214204.

[40] Y.L. Sun, J. Shen, A.A. Valladares, Atomic structure and diffusion in Cu60Zr40 metallic liquid and glass: molecular dynamics simulations, J. Appl. Phys. 106 (2009), 073520, https://doi.org/10.1063/1.3245324.

[41] N.A. Mauro, J.C. Bendert, A.J. Vogt, J.M. Gewin, K.F. Kelton, High energy x-ray scattering studies of the local order in liquid Al, J. Chem. Phys. 135 (2011), 044502, https://doi.org/10.1063/1.3609925.

[42] S. Trady, A. Hasnaoui, M. Mazroui, K. Saadouni, Local atomic structures of single-component metallic glasses, Eur. Phys. J. B 8910 (2016) (2016) 1–9, https://doi.org/10.1140/EPJB/E2016-60832-1, 89.

[43] N. Jakse, A. Pasturel, Coupling between dynamic slowing down and chemical heterogeneity in a metallic undercooled liquid, Phys. Rev. B 95 (2017) 144210, https://doi.org/10.1103/PhysRevB.95.144210.

[44] H.W. Sheng, W.K. Luo, F.M. Alamgir, J.M. Bai, E. Ma, Atomic packing and short-to-medium-range order in metallic glasses, Nature 439 (2006) 419–425, https://doi.org/10.1038/nature04421.

[45] Y.Q. Cheng, H.W. Sheng, E. Ma, Relationship between structure, dynamics, and mechanical properties in metallic glass-forming alloys, Phys. Rev. B Condens. Matter 78 (2008), https://doi.org/10.1103/PhysRevB.78.014207.

[46] T. Fukunaga, K. Itoh, T. Otomo, K. Mori, M. Sugiyama, H. Kato, M. Hasegawa, A. Hirata, Y. Hirotsu, A.C. Hannon, Voronoi analysis of the structure of Cu-Zr and Ni-Zr metallic glasses, Intermetallics 14 (2006) 893–897, https://doi.org/10.1016/j.intermet.2006.01.006.

[47] J. Wang, A. Agrawal, K. Flores, Are hints about glass forming ability hidden in the liquid structure? Acta Mater. 171 (2019) 163–169, https://doi.org/10.1016/j.actamat.2019.04.001.

[48] J. Ding, Y.Q. Cheng, H. Sheng, E. Ma, Short-range structural signature of excess specific heat and fragility of metallic-glass-forming supercooled liquids, Phys. Rev. B Condens. Matter 85 (2012), https://doi.org/10.1103/PhysRevB.85.060201.

[49] J. Ding, Y.Q. Cheng, E. Ma, Full icosahedra dominate local order in Cu64Zr34 metallic glass and supercooled liquid, Acta Mater. 69 (2014) 343–354, https://doi.org/10.1016/j.actamat.2014.02.005.

[50] X.W. Fang, C.Z. Wang, Y.X. Yao, Z.J. Ding, K.M. Ho, Atomistic cluster alignment method for local order mining in liquids and glasses, Phys. Rev. B Condens. Matter 82 (2010) 184204, https://doi.org/10.1103/PhysRevB.82.184204.

[51] X.W. Fang, C.Z. Wang, S.G. Hao, M.J. Kramer, Y.X. Yao, M.I. Mendelev, Z.J. Ding, R.E. Napolitano, K.M. Ho, Spatially resolved distribution function and the medium-range order in metallic liquid and glass, Sci. Rep. 1 (2011) 1–5, https://doi.org/10.1038/srep00194.

[52] Y. Sun, F. Zhang, Z. Ye, Y. Zhang, X. Fang, Z. Ding, C.Z. Wang, M.I. Mendelev, R. T. Ott, M.J. Kramer, K.M. Ho, Crystal genes' in metallic liquids and glasses, Sci. Rep. 6 (2016) 1–8, https://doi.org/10.1038/srep23734.

[53] A.D. Banadaki, J.J. Maldonis, P.M. Voyles, S. Patala, Point-pattern Matching Technique for Local Structural Analysis in Condensed Matter, 2018. http://arxiv.org/abs/1811.06098. (Accessed 22 October 2019).
[54] J.J. Maldonis, A.D. Banadaki, S. Patala, P.M. Voyles, Short-range order structure motifs learned from an atomistic model of a Zr50Cu45Al5 metallic glass, Acta Mater. 175 (2019) 35–45, https://doi.org/10.1016/j.actamat.2019.05.002.
[55] M. Li, C.Z. Wang, S.G. Hao, M.J. Kramer, K.M. Ho, Structural heterogeneity and medium-range order in Zrx Cu100-x metallic glasses, Phys. Rev. B Condens. Matter 80 (2009), https://doi.org/10.1103/PHYSREVB.80.184201/FIGURES/1/THUMBNAIL.
[56] K. Song, X. Bian, X. Lv, J. GuO, G. Li, M. Xie, Compositional dependence of glass-forming ability, medium-range order, thermal stability and liquid fragility of Al–Ni–Ce-based amorphous alloys, Mater. Sci. Eng. 506 (2009) 87–93, https://doi.org/10.1016/J.MSEA.2008.11.043.
[57] O.S. Roik, O.V. Samsonnikov, V.P. Kazimirov, V.E. Sokolskii, S.M. Galushko, Medium-range order in Al-based liquid binary alloys, J. Mol. Liq. 151 (2010) 42–49, https://doi.org/10.1016/J.MOLLIQ.2009.11.001.
[58] J. Kang, J. Zhu, S.H. Wei, E. Schwegler, Y.H. Kim, Persistent medium-range order and anomalous liquid properties of Al 1-xCu x alloys, Phys. Rev. Lett. 108 (2012), https://doi.org/10.1103/PHYSREVLETT.108.115901/FIGURES/1/THUMBNAIL.
[59] F. Zhang, M. Ji, X.W. Fang, Y. Sun, C.Z. Wang, M.I. Mendelev, M.J. Kramer, R. E. Napolitano, K.M. Ho, Composition-dependent stability of the medium-range order responsible for metallic glass formation, Acta Mater. 81 (2014) 337–344, https://doi.org/10.1016/J.ACTAMAT.2014.08.041.
[60] Z.W. Wu, F.X. Li, C.W. Huo, M.Z. Li, W.H. Wang, K.X. Liu, Critical scaling of icosahedral medium-range order in CuZr metallic glass-forming liquids, Sci. Rep. 61 (2016) 1–7, https://doi.org/10.1038/srep35967, 6 (2016).
[61] M.J. Kramer, M. Li, Changes in short- and medium-range order in metallic liquids during undercooling, MRS Bull. 45 (2020) 943–950, https://doi.org/10.1557/mrs.2020.272.
[62] J. Russo, H. Tanaka, The microscopic pathway to crystallization in supercooled liquids, Sci. Rep. 21 (2012) (2012) 1–8, https://doi.org/10.1038/srep00505, 2.
[63] J. Ding, E. Ma, Computational modeling sheds light on structural evolution in metallic glasses and supercooled liquids, Npj Comput. Mater. 31 (2017) 1–12, https://doi.org/10.1038/s41524-017-0007-1, 3 (2017).
[64] Y. Zhang, F. Zhang, C.Z. Wang, M.I. Mendelev, M.J. Kramer, K.M. Ho, Cooling rates dependence of medium-range order development in Cu64.5Zr35.5 metallic glass, Phys. Rev. B Condens. Matter 91 (2015), 064105, https://doi.org/10.1103/PhysRevB.91.064105.
[65] T.Q. Wen, L. Tang, Y. Sun, K.M. Ho, C.Z. Wang, N. Wang, Crystal genes in a marginal glass-forming system of Ni50Zr50, Phys. Chem. Chem. Phys. 19 (2017) 30429–30438, https://doi.org/10.1039/c7cp05976k.
[66] Y. Sun, Y. Zhang, F. Zhang, Z. Ye, Z. Ding, C.Z. Wang, K.M. Ho, Cooling rate dependence of structural order in Al90Sm10 metallic glass, J. Appl. Phys. 120 (2016), 015901, https://doi.org/10.1063/1.4955223.
[67] Y. Sun, F. Zhang, Z. Ye, Z. Ding, M.I. Mendelev, M.J. Kramer, C.Z. Wang, K.M. Ho, Structural ordering at solid-liquid interfaces in Al-Sm system: a molecular-dynamics study, Mater. Lett. 186 (2017) 26–29, https://doi.org/10.1016/j.matlet.2016.07.046.
[68] D. Wei, J. Yang, M.Q. Jiang, L.H. Dai, Y.J. Wang, J.C. Dyre, I. Douglass, P. Harrowell, Assessing the utility of structure in amorphous materials, J. Chem. Phys. 150 (2019) 114502, https://doi.org/10.1063/1.5064531.
[69] P. Tsai, K.M. Flores, A laser deposition strategy for the efficient identification of glass-forming alloys, Metall. Mater. Trans. A Phys. Metall. Mater. Sci. 46 (2015) 3876–3882, https://doi.org/10.1007/s11661-015-2900-x.
[70] Y. Li, Q. Guo, J.A. Kalb, C.V. Thompson, Matching glass-forming ability with the density of the amorphous phase, Science 322 (2008) 1816–1819, https://doi.org/10.1126/science.1163062 (80).
[71] D.C. Hofmann, G. Duan, W.L. Johnson, TEM study of structural evolution in a copper mold cast Cu 46Zr54 bulk metallic glass, Scripta Mater. 54 (2006) 1117–1122, https://doi.org/10.1016/j.scriptamat.2005.11.065.
[72] G. Duan, D. Xu, Q. Zhang, G. Zhang, T. Cagin, W.L. Johnson, W.A. Goddard, Molecular dynamics study of the binary Cu46Zr54 metallic glass motivated by experiments: glass formation and atomic-level structure, Phys. Rev. B Condens. Matter 71 (2005), https://doi.org/10.1103/PhysRevB.71.224208.
[73] D. Xu, B. Lohwongwatana, G. Duan, W.L. Johnson, C. Garland, Bulk metallic glass formation in binary Cu-rich alloy series - Cu 100-xZrx (x=34 , 36, 38.2, 40 at.%) and mechanical properties of bulk Cu64Zr36 glass, Acta Mater. 52 (2004) 2621–2624, https://doi.org/10.1016/j.actamat.2004.02.009.
[74] O.J. Kwon, Y.C. Kim, K.B. Kim, Y.K. Lee, E. Fleury, Formation of amorphous phase in the binary Cu-Zr alloy system, Met. Mater. Int. 12 (2006) 207–212, https://doi.org/10.1007/BF03027532.
[75] P. Tsai, K.M. Flores, A combinatorial strategy for metallic glass design via laser deposition, Intermetallics 55 (2014) 162–166, https://doi.org/10.1016/j.intermet.2014.07.017.
[76] B. Zhao, F. Zeng, F. Pan, Amorphization in the Ni-Nb system upon ion-beam-assisted deposition, Japanese J. Appl. Physics, Part 1 Regul. Pap, Short Notes Rev. Pap. 40 (2001) 5369–5372, https://doi.org/10.1143/jjap.40.5369.
[77] Z.M. Wang, J. Zhang, J.Q. Wang, Pit growth in a Ni-Nb metallic glass compared with its crystalline counterpart, Intermetallics 18 (2010) 2077–2082, https://doi.org/10.1016/j.intermet.2010.06.010.
[78] Y. Zhang, R. Ashcraft, M.I. Mendelev, C.Z. Wang, K.F. Kelton, Experimental and molecular dynamics simulation study of structure of liquid and amorphous Ni62Nb38 alloy, J. Chem. Phys. 145 (2016), https://doi.org/10.1063/1.4968212.
[79] J.C. de Lima, A.S. Ferreira, R.S. de Biasi, Modeling the amorphous structure of mechanically alloyed amorphous Ni30Nb70 using anomalous wide-angle X-ray scattering and reverse Monte Carlo simulations, J. Non-Cryst. Solids 447 (2016) 21–28, https://doi.org/10.1016/j.jnoncrysol.2016.05.027.
[80] A. Inoue, K. Ohtera, Z. Tao, T. Masumoto, New amorphous al-ln (ln=pr, nd, sm or gd) alloys prepared by melt spinning, Jpn. J. Appl. Phys. 27 (1988) L1583–L1586, https://doi.org/10.1143/JJAP.27.L1583.
[81] A. Inoue, Amorphous, nanoquasicrystalline and nanocrystalline alloys in Al-based systems, Prog. Mater. Sci. 43 (1998) 365–520, https://doi.org/10.1016/S0079-6425(98)00005-X.
[82] G. Wilde, H. Sieber, J.H. Perepezko, Glass formation versus nanocrystallization in an Al92Sm8 alloy, Scripta Mater. 40 (1999) 779–783, https://doi.org/10.1016/S1359-6462(99)00029-9.
[83] G. Wilde, H. Sieber, J.H. Perepezko, Glass formation in Al-rich Al-Sm alloys during solid state processing at ambient temperature, J. Non-Cryst. Solids 250–252 (II) (1999) 621–625, https://doi.org/10.1016/S0022-3093(99)00147-7.
[84] W.G. Stratton, J. Hamann, J.H. Perepezko, P.M. Voyles, X. Mao, S.V. Khare, Aluminum nanoscale order in amorphous Al92 Sm8 measured by fluctuation electron microscopy, Appl. Phys. Lett. 86 (2005) 1–3, https://doi.org/10.1063/1.1897830.
[85] G.B. Bokas, L. Zhao, J.H. Perepezko, I. Szlufarska, On the role of Sm in solidification of Al-Sm metallic glasses, Scripta Mater. 124 (2016) 99–102, https://doi.org/10.1016/j.scriptamat.2016.06.045.
[86] J. Weissmüller, Reduced short-range order in amorphous silicon-gold alloys, J. Non-Cryst. Solids 142 (1992) 70–80, https://doi.org/10.1016/S0022-3093(05)80008-0.
[87] A.P. Tsai, T. Kamiyama, Y. Kawamura, A. Inoue, T. Masumoto, Formation and precipitation mechanism of nanoscale Al particles in Al-Ni base amorphous alloys, Acta Mater. 45 (1997) 1477–1487, https://doi.org/10.1016/S1359-6454(96)00268-6.
[88] S. Plimpton, Fast Parallel algorithms for short-range molecular dynamics, J. Comput. Phys. 117 (1995) 1–19, https://doi.org/10.1006/JCPH.1995.1039.
[89] V. Borovikov, M.I. Mendelev, A.H. King, Effects of stable and unstable stacking fault energy on dislocation nucleation in nano-crystalline metals, Model. Simulat. Mater. Sci. Eng. 24 (2016), 085017, https://doi.org/10.1088/0965-0393/24/8/085017.
[90] L. Ward, A. Agrawal, K.M. Flores, W. Windl, Rapid Production of Accurate Embedded-Atom Method Potentials for Metal Alloys, 2012. http://arxiv.org/abs/1209.0619. (Accessed 29 June 2021).
[91] M.I. Mendelev, F. Zhang, Z. Ye, Y. Sun, M.C. Nguyen, S.R. Wilson, C.Z. Wang, K. M. Ho, Development of interatomic potentials appropriate for simulation of devitrification of Al90Sm10 alloy, Model. Simulat. Mater. Sci. Eng. 23 (2015), https://doi.org/10.1088/0965-0393/23/4/045013.
[92] S.V. Starikov, N.Y. Lopanitsyna, D.E. Smirnova, S.V. Makarov, Atomistic simulation of Si-Au melt crystallization with novel interatomic potential, Comput. Mater. Sci. 142 (2018) 303–311, https://doi.org/10.1016/j.commatsci.2017.09.054.
[93] L. Ward, D. Miracle, W. Windl, O.N. Senkov, K. Flores, Structural evolution and kinetics in Cu-Zr metallic liquids from molecular dynamics simulations, Phys. Rev. B Condens. Matter 88 (2013) 134205, https://doi.org/10.1103/PhysRevB.88.134205.
[94] A. Stukowski, Visualization and analysis of atomistic simulation data with OVITO-the Open Visualization Tool, Model. Simulat. Mater. Sci. Eng. 18 (2010).
[95] L. McInnes, J. Healy, S. Astels, hdbscan: hierarchical density based clustering, J. Open Source Softw. 2 (2017) 205, https://doi.org/10.21105/joss.00205.
[96] J.J. Maldonis, A.D. Banadaki, S. Patala, P.M. Voyles, Motif Extraction Github Page, (n.d.). https://github.com/paul-voyles/motifextraction.
[97] P. Weeks, Liquid Structure Analysis Github Repository, (n.d.). https://github.com/weekswp/liquid_structure_analysis.
[98] T. Wang, F. Zhang, L. Yang, X.W. Fang, S.H. Zhou, M.J. Kramer, C.Z. Wang, K. M. Ho, R.E. Napolitano, A computational study of diffusion in a glass-forming metallic liquid, Sci. Rep. 5 (2015) 10956, https://doi.org/10.1038/srep10956.
[99] S.H. Zhou, R.E. Napolitano, The stability of Al11Sm3 (Al4Sm) phases in the Al-Sm binary system, Metall. Mater. Trans. 38 (2007) 1145–1151, https://doi.org/10.1007/s11661-007-9148-z.
[100] S.H. Zhou, R.E. Napolitano, Modeling of thermodynamic properties and phase equilibria for the Al-Sm binary system, Metall. Mater. Trans. 39 (2008) 502–512, https://doi.org/10.1007/s11661-007-9445-6.